EFFECTS OF MAGNETIC TOPOLOGY ON CME KINEMATIC PROPERTIES

Wei Liu[(1)], Xue Pu Zhao[(1)], S. T. Wu[(2)], Philip Scherrer[(1)]

[(1)]W. W. Hansen Experimental Physics Laboratory, Stanford University, Stanford, CA 94305-4085, USA, Email: weiliu@quake.stanford.edu

[(2)]Center for Space Plasma and Aeronomic Research and Department of Mechanical & Aerospace Engineering, The University of Alabama in Huntsville, Huntsville, AL 35899, USA, Email: wus@cspar.uah.edu

ABSTRACT

Coronal Mass Ejections (CMEs) exhibit two types of kinematic property: fast CMEs with high initial speeds and slow CMEs with low initial speeds but gradual accelerations. To account for this dual character, [1] (hereafter LZ2002) proposed that fast and slow CMEs result from initial states with magnetic configurations characterized by normal and inverse quiescent prominences, respectively. To test their theory and further explore the effects of topology on the kinematic properties of CMEs we employed a self-consistent magnetohydrodynamic (MHD) model [2, 3] to simulate the evolution of CMEs respectively in the normal and inverse prominence environments. The numerical results show that CMEs originating from a normal prominence environment do have higher initial speeds than those from an inverse one. In addition, our simulations demonstrate the distinct roles played by magnetic reconnection in these two topologically different magnetic environments to produce the two different CME height-time profiles as suggested by LZ2002.

1. INTRODUCTION

It is known from observations made by coronagraphs on-board space missions such as Skylab, Solar Maximum Mission, Solwind, and most recently Solar and Heliospheric Observatory (SOHO) and from ground-based coronagraphs at Mauna Lao, that there are two distinct characteristic speed-height profiles of Coronal Mass Ejections (CMEs) [4, 5, 6, 7], in which CMEs originating from active regions and being accompanied by flares usually have initial speeds well above the CME median speed (400 km s^{-1}) in the low corona, and others originating away from active regions and accompanied by eruptive prominences show gradual accelerations with initial speeds less than the medium speed. Slow CMEs have been simulated by [3, 8] using an inverse prominence magnetic field configuration. These simulations agree well with specific events observed by the SOHO/LASCO coronagraph [9]. A variety of efforts have been made to probe the underlying physics responsible for these dual characteristics. Recently, LZ2002 has proposed a theoretical model based on observed magnetic topologies of quiescent prominences, which exhibit two distinct types, i.e., normal and inverse prominence configurations. A normal prominence magnetic configuration is defined as having the magnetic field thread across the prominence in the same direction as the field contributed by the bipolar photospheric region below. An inverse prominence configuration has the opposite direction with respect to a normal one [10]. On the basis of these topologies, LZ2002 proposed their theory to explain the dual kinematic characteristics of CMEs as follows. In the case of the normal configuration, a current sheet forms above the flux rope. Magnetic reconnection there removes the flux from the overlying closed magnetic field and the resulting magnetic configuration expels the rope energetically. This corresponds to the class of CMEs with high initial speeds low in the corona. In the case of the inverse configuration, a current sheet forms below the rising flux rope. Magnetic reconnection does not play a principal role in launching the CME [3, 9] and the constraints from the overlying field tend to confine the flux rope as well. This results in CMEs that experience gradual accelerations with low initial speeds.

LZ2002's theoretical scenario has been supported by recent observations [11]. However, it lacks quantitative arguments. Aiming to fill this gap, we present in this paper a 2-D, time-dependent, resistive magnetohydrodynamic (MHD) simulation to test their theory. The description of our mathematical model and physical parameters are given in Section 2. The numerical results are described in Section 3. Finally, Section 4 contains the concluding remarks.

2. MATHEMATICAL MODEL

To investigate CMEs in different magnetic topologies, we adapted the method given by [3] to emerge topologically different magnetic bubbles (2-D counterparts of 3-D magnetic flux ropes) into a coronal helmet streamer, with details described as follows.

The coronal plasma was modelled with the single-fluid MHD equations. We took into account resistivity to

allow reconnection and accordingly modified the magnetic induction equation and energy equation in [3] as,

$$\frac{\partial \boldsymbol{B}}{\partial t} = \nabla \times (\boldsymbol{u} \times \boldsymbol{B}) - \nabla \times (\eta \boldsymbol{J}), \qquad (1)$$

and

$$\frac{\partial T}{\partial t} = -\nabla \cdot (T\boldsymbol{u}) + (2-\gamma) T \nabla \cdot \boldsymbol{u} + \frac{\gamma - 1}{\rho R} \eta |\boldsymbol{J}|^2, \quad (2)$$

where η is the magnetic resistivity which we set to be a constant, $\boldsymbol{J} = \nabla \times \boldsymbol{B}/\mu_0$ is the current density, and R the gas constant; other quantities have their commonly-used meanings.

The computational domain lies in the meridional plane, with the radial extension $1R_s \le r \le 7.14R_s$, where R_s is the solar radius, and the latitudinal extension $-1.5° \le \theta \le 91.5°$, where the pole (equator) is located at 0° (90°). This domain was discretized into an 81 (r) × 63 (θ) mesh. To achieve better spatial resolution near the sun, we chose the grid spacing in the r-direction to increase as a geometric series, $\Delta r_i = r_{i+1} - r_i = 0.025 r_{i-1}$, and uniform in the θ-direction, $\Delta\theta = 1.5°$.

The MHD equations were cast in a two-dimensional spheric form ($\partial/\partial\phi = 0$ and all the ϕ-components are zero) and solved by the combined difference technique [3] which employs different numerical schemes to treat different equations according to their physical nature, namely, (i) the second type upwind scheme is used for the continuity and energy equation; (ii) the Lax scheme for the momentum equation; (iii) the Lax-Wendroff scheme for the magnetic induction equation. A staggering net was adopted to achieve high accuracy and avoid sawtooth oscillations. To guarantee the solenoidal condition of the magnetic field, i.e. $\nabla \cdot \boldsymbol{B} = 0$, we applied the reiterative divergence-cleaning method in each time step [12].

The method of projected normal characteristics [13] was adopted to treat the boundary conditions. At the inner boundary, u_r and B_θ were calculated with the characteristic boundary condition; u_θ was obtained with the $\boldsymbol{u} \| \boldsymbol{B}$ condition; the remaining dependent variables, B_r, ρ, and T were fixed. Linear extrapolations were used at the outer boundary since the flow there is supersonic and super-Alfvénic. At the equator and the pole, symmetric boundary conditions were imposed.

We took three steps, following [3], to model a CME as the response of the corona to the emergence of a current-bearing magnetic bubble. The first step was to construct a quasi-equilibrium corona with the background solar wind and a helmet streamer over the equator, using the relaxation method [14], as shown in Fig. 1. The characteristic plasma parameters are listed in Table I, in which all the quantities, except the solar wind speed, are evaluated at the equator and the inner boundary.

Table I. Characteristic parameters in the initial state

n_0	(electron number density)	3.2×10^8 cm^{-3}
T_0	(temperature)	1.8×10^6 K
B_o	(magnetic induction strength)	2.0 G
β_o	(plasma β)	1.0
c_s	(sound speed)	176.7 km/s
v_A	(Alfvén speed)	243.9 km/s
v_{sw}	(solar wind speed at 7.14 R_s on the equatorial plane)	209.7 km/s

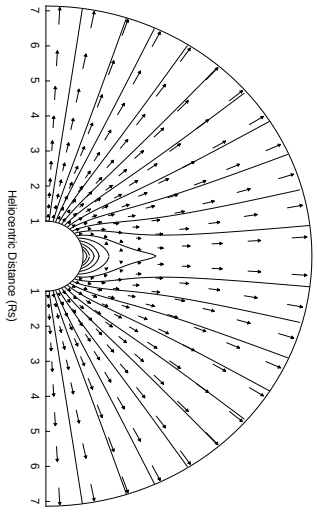

Fig. 1. The MHD solution of the magnetic field lines and solar wind velocity for the initial helmet streamer.

In the second step, we moved a current-carrying magnetic bubble from below the photosphere into the corona. The solution for a cross-section of an axisymmetric cylinder of radius a containing a volumetric current in equilibrium is given in local cylindrical coordinates (r', θ') as (see [3]):

$$\boldsymbol{B}(r') = \pm\mu_0 j_0 \left(\frac{1}{2} a r' - \frac{1}{3} r'^2 \right) \boldsymbol{e}_{\theta'}, \qquad (3)$$

$$p(r') = p_0 + \mu_0 j_0^2 \left(\frac{1}{18}a^4 - \frac{1}{4}a^2 r'^2 + \frac{5}{18}a r'^3 - \frac{1}{12}r'^4 \right), \quad (4)$$

where

$$j_0^2 = \frac{18(m-1)p_0}{\mu_0 a^4}, \quad (5)$$

and p_0 is the plasma pressure at the inner boundary ($r = R_s$). Note that the "±" in Eq. 3 represents different sense of circulation of the magnetic field lines inside the bubble. A bubble with a "+" ("–") has the same (opposite) sense in the direction of the magnetic field in its upper half with respect to the bipolar field in the background corona. This distinction corresponds to the inverse and normal magnetic topology of prominences, respectively, in LZ2002's theory, which can be appreciated in the following sections of this paper. To emerge the bubble, we first placed the bubble below the photosphere with its center at $r = R_s - a$, and then displaced the bubble upward at a constant speed (see Column 5 in Table II) by accordingly changing the values of the velocity, pressure, and magnetic field at the inner boundary. It took 4 hours for the bubble to completely emerge into the corona.

The last step was carried out by letting the system evolve by itself governed by the full set of MHD equations. We present the numerical results in next section.

3. NUMERICAL RESULTS

Eight cases with different size and different energy content of the emerging magnetic bubble were run to study the temporal evolution of CMEs. These cases are arranged in a pair-wise manner. Each pair consists of two types of magnetic topology that have opposite magnetic polarities of the magnetic bubble; otherwise conditions are identical. These magnetic topologies represent the inverse and normal prominence configuration respectively as described above. Key parameters of these cases are listed in Table II.

From these numerical results we immediately recognise the importance of the initial magnetic topology on the eruption. For instance, in cases 1a and 2a, we notice that the emerging bubble has already destabilized the streamer and launched a CME for the normal magnetic configuration. On the other hand, the streamer and the bubble are still in equilibrium for the inverse magnetic configuration (i.e. cases 1b and 2b), which can be clearly seen from the height-time and speed-time profiles in Fig. 2. It is also interesting to note that the ratio of the average speeds of case 4a to 4b is about 2.3 which agrees quite well with the observed fast-to-slow ratio of two-class CME speeds [4, 6].

Table II. Characteristics of Studied Cases

cases	a [1] (R_s)	flux-rope energy [2] (10^{31} erg)	emerg. speed [3] (km/s)	field topology	final eruption speed [4] (km/s)	average eruption speed [5] (km/s)
1a	0.10	1.76	9.7	Normal	174.6	90.0
1b				Inverse	0.1	1.0
2a	0.15	3.95	14.5	Normal	215.8	133.9
2b				Inverse	0.2	1.5
3a	0.20	7.02	19.3	Normal	253.6	152.6
3b				Inverse	88.0	9.3
4a	0.25	10.9	24.2	Normal	258.0	161.0
4b				Inverse	227.6	70.4

1) a: flux rope radius.
2) The combination of thermal and magnetic energy in the volume of the rope, assuming the 3rd-dimensional thickness $\Delta z = 0.1\ R_s$.
3) The bubble emergence speed in step 2 as described in the text.
4) and 5) represent the radial speed of the center of the "bubble", which refers to the original bubble in an inverse configuration or the newly formed bubble in a normal configuration.
4) is evaluated at the end of the simulation (t = 40 hrs).
5) is averaged over the interval during which the bubble center remains in the computational domain (i.e., $1R_s \le r \le 7.14R_s$).

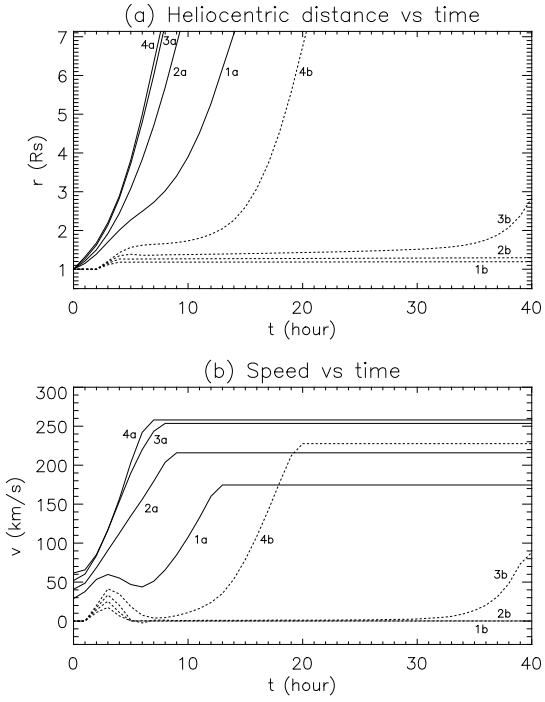

Fig. 2. The height-time (a) and speed-time (b) profiles for the eight cases listed in Table II. Note for some speed profiles: the initial humps at t ≅ 3 hrs are introduced by emerging the bubble into the corona, and the final flat portions are extrapolations of the speeds evaluated at the outer boundary ($r = 7.14\ R_s$).

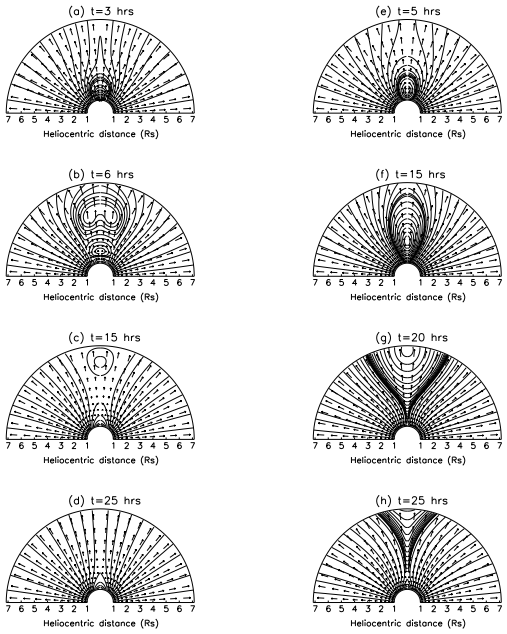

Fig. 3. The evolution of the magnetic field and plasma flow velocity for the normal (case 4a, left column) and inverse (case 4b, right column) magnetic topology.

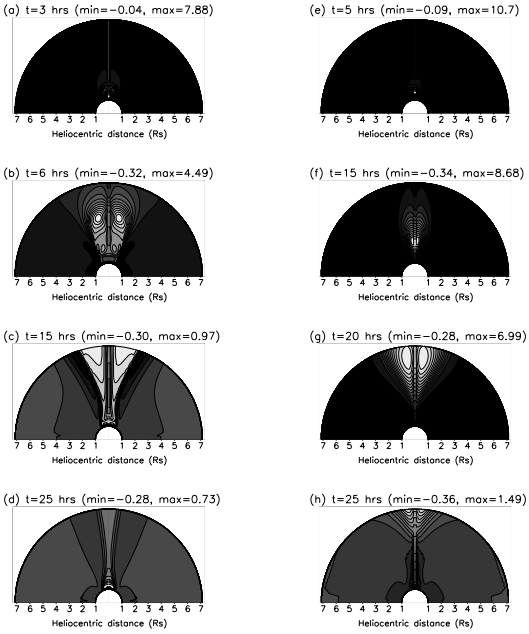

Fig. 4. The corresponding density enhancement of Fig. 3 (bright: high, dark: low). The left column represents the normal configuration (case 4a) and right column the inverse (case 4b). The minima and maxima are shown at the top of each panel and the interval [min, max] is evenly divided into 15 contour levels.

Now let us focus our attention on the typical eruptive cases 4a and 4b. Fig. 3 shows the magnetic field and the affected solar wind plasma velocity for the normal (left) and inverse (right) magnetic configuration. By examining the normal configuration, we notice that upon the emergence of the magnetic bubble (i.e. the cross-section of a flux rope) into the corona inside a streamer, a new bubble is rapidly formed. This process occurs immediately when the leading edge of the bubble touches the helmet streamer's closed bipolar magnetic field (which is anchored on the photosphere and opposite in direction to the field in the upper half of the bubble) and a current sheet is consequently formed, introducing magnetic reconnection there. This new bubble then grows in magnetic flux until all the closed-field flux in the streamer is converted by reconnection to the new bubble's flux, thus removing the constraints that tend to keep the original flux rope from erupting. Meanwhile, the new bubble expands in size and runs upward very fast, while the old one follows and loses an equal amount of magnetic flux as the streamer's closed field ahead. We identify the new bubble as the main body of a CME in this numerical experiment and the "average" and "final" speed in Table II refer to the speed of the new bubble's center (i.e., the O-type neutral point). At t = 25 hrs, the erupting material has escaped from the computational domain ($r > 7.14\ R_s$) and the system returns to a quasi-equilibrium state similar to the initial one (Fig. 1). The corresponding evolution of the density enhancements (i.e. $(\rho - \rho_0)/\rho_0$) is shown in Fig. 4 (left column), which resembles a typical three-part CME structure.

In the case of the inverse magnetic configuration (case 4b), the evolution of the magnetic field and plasma velocity is shown in the right column of Fig. 3. From these results it is clearly noted that there is no reconnection at the leading edge of the bubble. However, when the bubble rises, a vertical current sheet is formed at its trailing edge. Magnetic reconnection ensues and dissipates the sheet to re-close the magnetic field opened by the eruption. Therefore, it enables the system to reach another quasi-equilibrium state similar to the initial configuration as shown in Fig. 1 at 40 hrs (not shown). It is interesting to note that the recovery to equilibrium is much faster for the normal field configuration than that for the inverse one. This is probably due to the different CME propagation speeds for these two magnetic topologies. The speed-time profiles (Fig. 2) show a gradual acceleration starting at $t \cong 7$ hrs for the case of the inverse magnetic configuration, in contrast with that of the normal one.

Finally, in Fig. 5 we show the distributions of the radial components of forces (i.e. Lorentz force, pressure force, and gravitational force) at various times. By examining these results, we notice some interesting features: (i) for the normal magnetic configuration, the pressure force is the dominant positive force to destabilize the streamer in the initial stage (< 4 hrs) but it drops significantly afterwards.

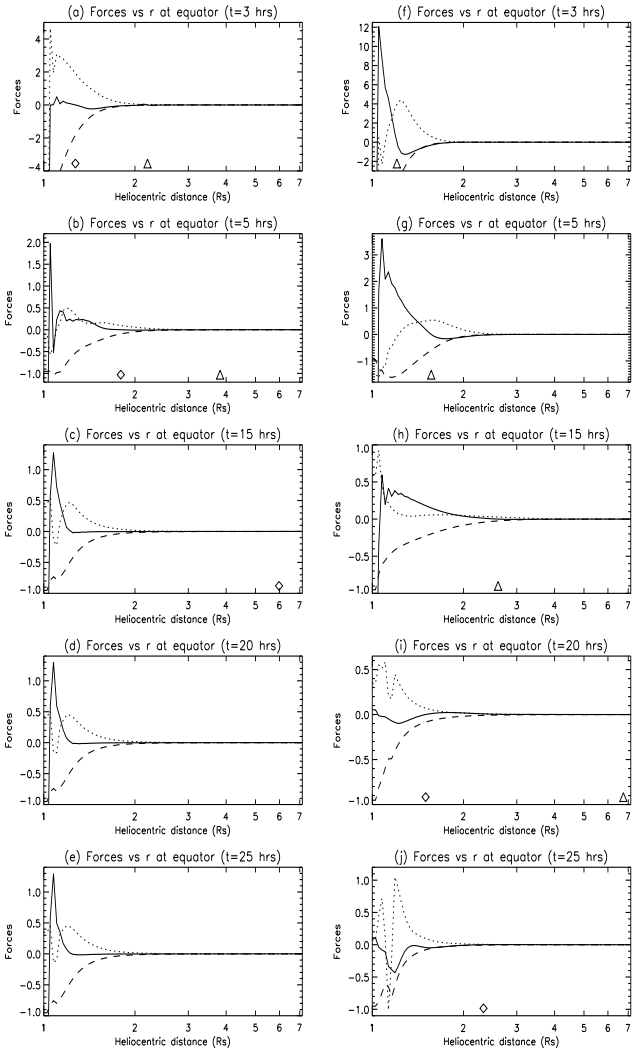

Fig. 5. Radial forces (i.e., Lorentz force ——, pressure force ·····, and gravitational force ------) per unit volume as a function of the heliocentric distance in the equatorial plane at various times for normal (left) and inverse (right) magnetic field configuration. Distance is logarithmically plotted to show details close to the solar surface. All the forces are normalized by the gravitational force at the equator on the photosphere in the initial state. Close to the bottom of each panel, diamond (triangular) symbols denote the radial positions of the higher (lower) neutral point.

This is true because it takes four hours (as we previously stated) to move the bubble, which carries substantial upward momentum, into the streamer and a large pressure force is accordingly developed. After that there is no additional momentum being added to the system. (ii) For the inverse configuration, the Lorentz and pressure force are somewhat comparable in the initial stage and they work together against the gravity to lift off the bubble material. Once the bubble emergence is complete (> 4 hrs), the Lorentz force takes over the dominance. This occurs probably for two reasons: on the one hand the pressure force decreases as in the normal configuration; on the other, the emerging bubble bears current in the same direction as that of the helmet streamer and this injected current produces an additional Lorentz force as a result of its interaction with the background magnetic field. The resulting Lorentz force is mainly responsible for the gradual acceleration of the bubble after $t \cong 7$ hrs (see Fig. 2) and leads to its eventual eruption. (iii) It is further noticed that during the eruption phase (i.e., before the bubble escapes from the domain) the magnitude of the positive Lorentz force about the bubble center for the normal configuration is much smaller than that for the inverse one at the same time. The reader is reminded that the electric current of the emerging bubble in the normal case runs oppositely to the current of the streamer. The interplay of the two current systems diminishes the net current and results in a lower Lorentz force.

Bearing the above features in mind, the reader may raise a question why the flux rope erupts faster in the normal magnetic configuration than in the inverse one. We propose that, in the normal configuration case, magnetic reconnection plays a direct role in launching the CME by forming the new magnetic bubble and removing the streamer's closed field lines as well as their constraints ahead of the original bubble, thereby allowing the bubbles to escape freely. However, in the case of the inverse configuration the overlying magnetic arcades tend to confine the bubble; lacking mechanisms (e.g., reconnection) to remove the confinement, the bubble thus could not reach higher initial speed, even though there is larger positive (driving) Lorentz force available. This argument can be appreciated by noting that the magnitude of the negative (confining) Lorentz force in the upper part of the bubble in the inverse case is much larger than its counterpart in the normal one (Fig. 5).

4. CONCLUDING REMARKS

We have presented a numerical MHD simulation to investigate the effects of the magnetic topology on CME kinematic properties. The results obtained from our simulation for the normal and inverse magnetic field configuration reveal that: (i) the CMEs resulting from a normal configuration indeed have higher initial speeds lower in the corona, in contrast with those from an inverse one; (ii) the ratio of the average CME speeds for these two types of configuration is about 2.3, which is consistent with observations; (iii) magnetic reconnection plays a principal role in launching a fast CME with a rapid initial acceleration in a normal magnetic configuration by removing the closed magnetic field lines.

In summary, the present simulation agrees well with LZ2002's model. Two types of magnetic topology lead to quite distinct kinematic properties of CMEs. However, the current numerical results have failed to demonstrate the observed demarcation line between the fast and slow CMEs, although the speed ratio of these two types matches with observations. This deficiency may be removed by seeking low-β MHD solutions and consequently increasing the energy content, or by upgrading this 2-D simulation to a 2.5-R or full 3-D model. These scenarios would be beyond the scope of the present paper and we look forward to future work to develop them.

5. ACKNOWLEDGEMENT

The authors would like to thank Dr. E. Tandberg-Hanssen for reading this manuscript and his valuable comments. W. Liu acknowledges with gratitude enlightening discussions with Dr. B. C. Low and M. Zhang and their kind hospitality during his visit to HAO. Work performed by WL, XPZ and PS was supported at Stanford University by NASA grants NAGW 2502, NAG5-3077, NSF grant (ATM9400298) and ONR grant (N0014-97-1-0129). Work performed by STW was supported by NASA grant NAG5-12843 and NSF grant ATM-0070385.

6. REFERENCES

1. Low, B. C. and Zhang, M., *Astrophys. J.*, Vol. 564, L53, 2002.

2. Guo, W. P., Wu, S. T., and Tandberg-Hanssen, E., *Astrophys. J.*, Vol. 469, 944, 1996.

3. Wu, S. T., Guo, W. P., and Wang, J. F., *Solar Phys*., Vol. 157, 325, 1995.

4. Gosling, J. T., et al., *Solar Phys*., Vol. 48, 389, 1976.

5. MacQueen, R. M. and Fisher, R. R., *Solar Phys*., Vol. 89, 89, 1983.

6. St. Cyr, O. C., et al., *J. Geophys. Res*., Vol. 104, 12493, 1999.

7. Andrews, M. D. and Howard, R. A., *Space Sci. Rev.*, Vol. 95, 147, 2001.

8. Wu, S. T., Guo, W. P., and Dryer, M., *Solar Phys*., Vol. 170, 265, 1997.

9. Wu, S. T., et al., *Solar Phys*., Vol. 175, 719, 1997.

10. Tandberg-Hanssen, E., *The Nature of Solar Prominences* (Dordrecht: Kluwer), 1995.

11. Zhang, M., et al., *Astrophys. J.*, Vol. 574, L97, 2002.

12. Ramshaw, J. D., *J. Comp. Phys.*, Vol. 52, 592, 1983.

13. Wu, S. T., and Wang, J. F., *Comp. Method Applied Mech. Eng*., Vol. 64, 267, 1987.

14. Steinolfson, R. S., Suess, S. T., and Wu, S. T., *Astrophys. J.*, Vol. 255, 730, 1982.